metals

MDPI

Article

Evolution of Mechanical Twinning during Cyclic Deformation of Mg-Zn-Ca Alloys

Alexei Vinogradov [1,*], Evgeny Vasilev [2], Mikhail Linderov [2] and Dmitry Merson [2]

[1] Department of Engineering Design and Materials, Norwegian University of Science and Technology—NTNU, N-7491 Trondheim, Norway

[2] Institute of Advanced Technologies, Togliatti State University, Belorusskaya str., 14, Togliatti 445667, Russia; evg.vasilyev11@gmail.com (E.V.); dartvi@gmail.com (M.L.); d.merson@tltsu.ru (D.M.)

* Correspondence: alexei.vinogradov@ntnu.no; Tel.: +47-735-93769

Academic Editors: Victor Hugo C. de Albuquerque and João Manuel R. S. Tavares

Received: 19 October 2016; Accepted: 29 November 2016; Published: 2 December 2016

Abstract: The present study clarifies the complex interplay between mechanical twinning and dislocation slip during low-cycle fatigue testing of Mg-Zn-Ca alloys. Temporal details of these mechanisms are studied non-destructively by in situ monitoring of the acoustic emission (AE) response powered by a robust signal categorization. Through the analysis of AE time series, the kinetics of deformation twinning per cycle and the overall accumulation of twinning during cyclic loading is described and its effect on fatigue life is highlighted.

Keywords: magnesium; twinning; dislocation slip; cyclic deformation; acoustic emission

1. Introduction

Microstructure and properties of magnesium and its alloys are the focus of numerous investigations nowadays owing to their being lightweight and recent developments in the processing technologies [1]. Specifically, magnesium and its alloys are promising for medical applications due to their unique combination of elastic properties, lightweight quality, biocompatibility and biodegradability [2,3]. However, for biomedical applications, they have to meet many challenging mechanical, electrochemical and biological requirements. The Mg-Zn-Ca alloy system has been proven, offering a very attractive combination of functional properties including a reasonably high strength and ductility [4–7]. The strength and corrosion resistance can improve with small additions of Ca in Mg-Zn systems. Besides the strength and ductility, fatigue properties and the cyclic response of Mg alloys are of significant interest. However, the cyclic behavior of Mg alloys in general and of Mg-Zn-Ca in particular has been investigated just scarcely. Tremendous experimental and theoretical efforts have been invested in the past two decades in understanding the processes governing plastic deformation in Mg and its alloys with different initial texture [8–15] under various loading conditions [16,17]. Plastic deformation of Mg and its alloys at room temperature occurs primarily by basal <a> slip $\{0001\}\langle 11\bar{2}0\rangle$ and extension twinning $\{10\bar{1}2\}\langle 10\bar{1}1\rangle$, which is activated by a tensile stress component along the *c*-axis [8]. Although the {10–11} contraction twins may appear in the non-texturized alloys investigated in this work, they are commonly featured by a higher critical resolved shear stress (CRSS) [9] and a low growth rate. Therefore, their contribution to strain accommodation is limited, and we do not discriminate between the two types twinning in the further analysis in this work. Upon reversal of the load direction, the twins shrink due to the motion of twin boundaries in opposite direction (de-twinning) and can disappear completely [18,19]. Deformation twinning involves two steps: nucleation and growth of twin lamellae. De-twinning is associated with twin shrinkage. Due to the polar nature, the twinning/de-twinning behavior exhibits pronounced asymmetry with respect to the direction of loading [8,9,20,21]. Paired with the asymmetry of tension-compression behavior

of twinning, this brings significant complexity to the overall cyclic response of Mg alloys. The latter is the subject of extensive research nowadays [22,23]. However, it is premature to say that cyclic properties and the mechanisms controlling them have been understood. One of the issues, which remains unclear in view of the above highlighted complexity, is how the twinning evolves and affects the cyclic hardening response in Mg alloys before crack initiation. This issue we endeavor to address in the present work with aid from the non-destructive in situ monitoring of the acoustic emission (AE) generated by plastic deformation mechanisms during symmetrical push-pull testing of Mg alloys.

Despite a large body of experimental investigations, the kinetics of asymmetrical behavior of twinning is still far from being understood comprehensively. AE has long been recognized as a powerful tool for the investigation and characterization of the deformation mechanisms on different time scales. The main advantages of the method are the high time resolution and sensitivity to twin nucleation and collective dislocation motion [24]. The AE signal processing has experienced revolutionary changes with the advent of computer and information technologies in recent years. A novel statistical method of AE signal categorization and recognition developed in [25] has been proven effective for real-time analysis of elementary deformation mechanisms in advanced materials including Mg alloys. The method was successfully tested and applied for discrimination between contributing deformation mechanisms such as dislocation slip, twinning and martensitic transformations from the AE signal at various stages of deformation in several materials [26–30]. In the present work, we extend the proposed technique to low-cycle fatigue deformation to failure aiming at exploring its capacity of for non-destructive characterization of deformation processes in complex alloy systems where multiple deformation mechanisms are involved.

2. Experimental Section

Commercial purity ZX40 series Mg-Zn-Ca alloys with nominal compositions 4Zn-0.16Ca-Mg and 4Zn-0.56Ca-Mg (all in wt %) were gravity cast and subjected to a thermomechanical treatment involving annealing at 330 °C for 24 h followed by equal-channel angular pressing (ECAP) through the round 10 mm diameter channels intersecting at 120 degrees. One pressing through the die was performed at 320 °C.

The metallography specimens were polished down to 0.25 μm and then etched in a solution containing 50 mL distilled water, 150 mL ethanol and 1 mL acetic acid, Figure 1a. Microstructural observation was carried out using an optical microscope Zeiss Axiovert (Ulm, Germany) with the image analyzing software Thixomet™ (Thixomet, St. Petersburg, Russia) and a field emission gun scanning electron microscope (SEM) Zeiss SIGMA (Ulm, Germany) equipped with an EDAX/TSL (Mahwah, UK) energy dispersive X-ray (EDX) spectrometer.

Mechanical testing was carried out using a rigid electro-dynamic testing machine Instron Electropulse E1000 (Instron, High Wycombe, UK). Having a silent drive mechanism, this machine ensured a very low mechanical noise in the frequency band from 150 to 600 kHz and lack of interference with the AE measuring system. Cyclic tests were conducted on ECAP-ed flat I-shaped sub-size specimens having the gauge dimensions of $5 \times 2 \times 2$ mm^3 shown in the inset in Figure 2a. The specimens were cut by spark erosion and then mechanically polished to a mirror finish. They were subjected to axial push-pull deformation cycles under total strain control with a feedback signal from the Epsilon™ (Epslion Technology, Jackson, MS, USA) NT-3442 extensometer. A sine wave controlling signal was applied at 0.2 Hz.

A miniature broadband AE sensor PICO (Physical Acoustics, Princeton, NJ, USA) was mounted securely on an unstrained shoulder part in close proximity to the gauge part (see the inset in Figure 2). The signal was amplified by 60 dB by the MSAE-F1 (Microsensors AE, Sarov, Russia) preamplifier and then transferred to the PC-controlled AE-recording system based on the PCI-2 data acquisition board. AE recording was performed in a threshold-less mode at a sampling rate of 2 MHz. The continuously streamed data were sectioned into consecutive individual realizations ("frames") of 4 k samples without overlapping. A Fourier power spectral density (PSD) function $G(f)$ was calculated

from these data using a Welch technique. The AE power (often termed "energy") was calculated from the corresponding PSD $E = \int_{f_{\min}}^{f_{\max}} G(f)df$ and the median frequency f_{m} of the PSD function was introduced as $\int_0^{f_{\mathrm{m}}} G(f)df = \int_{f_{\mathrm{m}}}^{\infty} G(f)df$ [31]. The AE data set was analyzed employing the signal categorization technique—adaptive sequential *k*-means clustering (ASK)—proposed in [25]. The normalized PSD function $\widetilde{G}(f) = G(f)/E$ were used as input for the ASK algorithm, which compares the difference between them using a symmetrical version of the Kulback-Leibler divergence as a statistical measure of similarity between two data sets. Further details of the AE experimental setup can be found in [26,32].

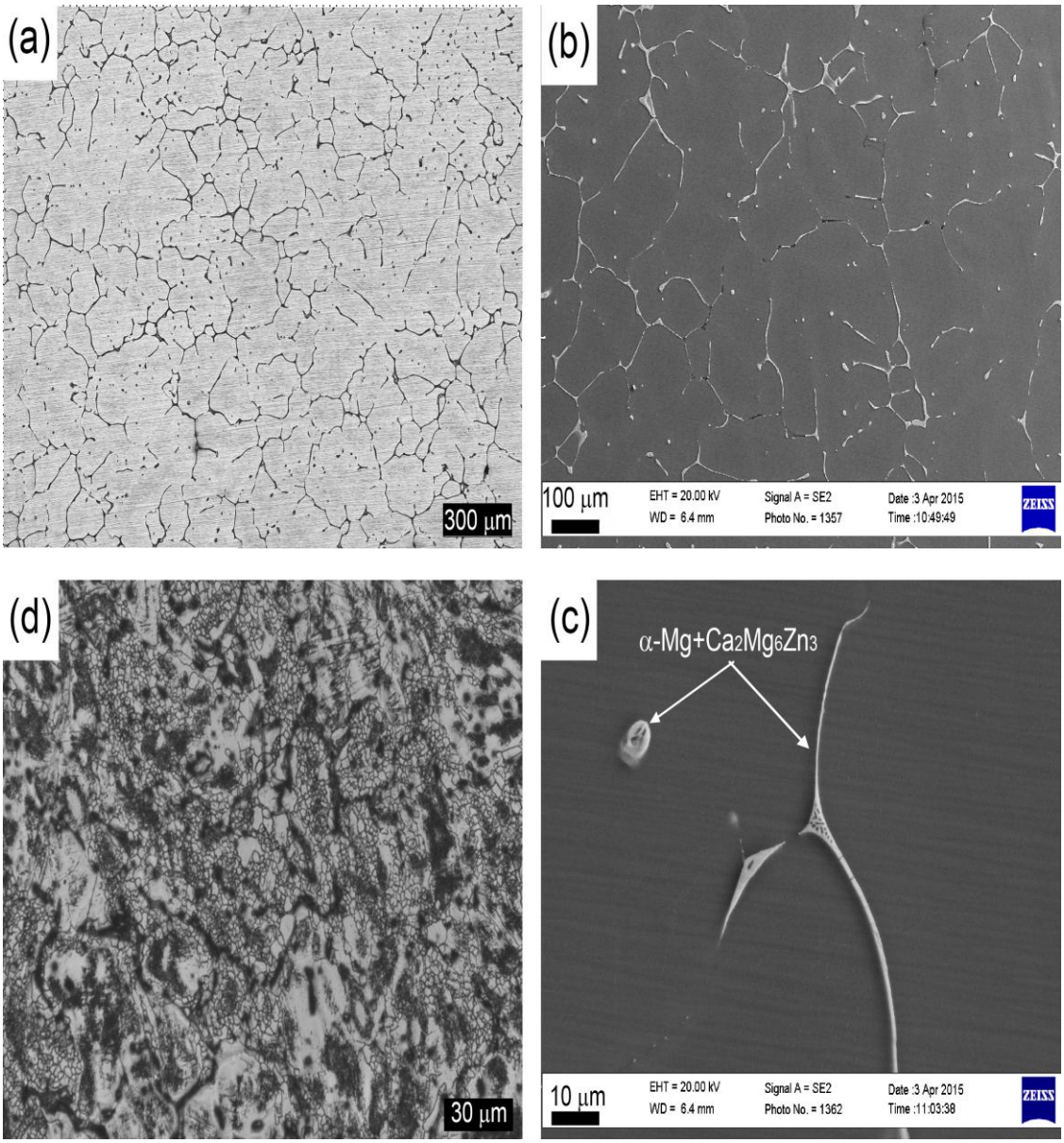

Figure 1. Optical (**a**); and SEM (**b**); and (**c**) micrographs showing a phase structure of the as-cast ZX40 Mg-4Zn-0.16Ca alloy; (**d**) the same alloy after Equal Channel Angular Pressing (ECAP).

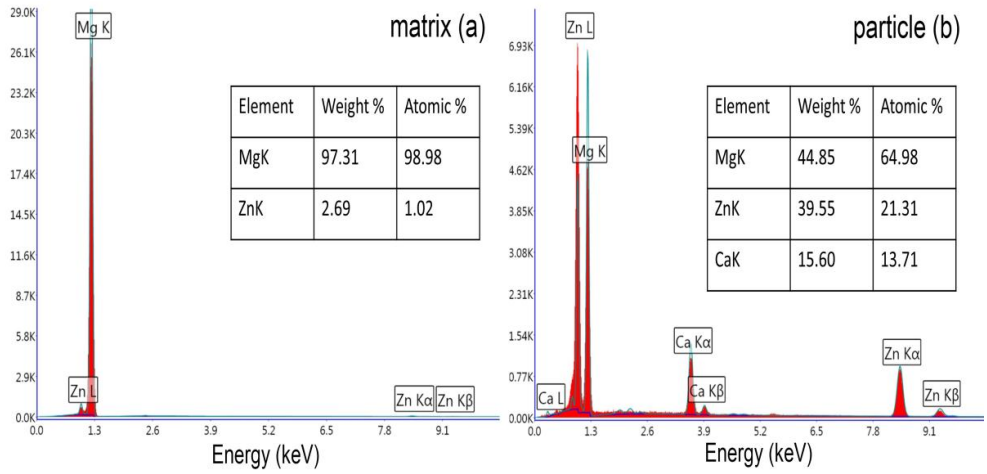

Figure 2. Energy Dispersive X-ray (EDX) spectra obtained from the α-Mg matrix (**a**); and the secondary phase particle (**b**) in the as cast Mg-4Zn-0.16Ca alloy.

3. Results and Discussion

From Mg-Ca binary phase diagram, the maximum solubility of Ca in Mg at 516.35 °C is 1.34 wt %, about 0.4 wt % at 350 °C and only 0.2 wt % at room temperature [33–35]. The literature shows contradicting information regarding the ternary compounds in the Mg-Zn-Ca system. The phase formation and microstructure evolution during solidification, solution treatment and ageing of an Mg-Ca-Zn alloy have been predicted qualitatively and quantitatively based on computational thermodynamics by many authors, e.g., [36–39]. Wasiur-Rahman and Medraj [39] performed the critical assessment of the experimental data accumulated to date in line with thermodynamic modeling of phase equilibria to determine the most likely description of this system and to eliminate the self-contradicting experimental observations. The consideration of the two ternary compounds reported by Clark—$Ca_2Mg_6Zn_3$ and $Ca_2Mg_5Zn_{13}$—resulted in the best consistency with the experimental results reported in the literature, e.g., [33]. Bakhsheshi-Rad et al. [38] investigated the influence of Zn content on the microstructure, phase compositions and corrosion resistance of binary Mg-*x*Zn and ternary Mg-0.8Ca-*x*Zn (x = 1.25, 2.5, 4 wt %) alloys. The effect of the Ca content in Mg-4Zn-*x*Ca (x = 0.18–2.2 wt %) on the microstructure, phase composition and morphology has been systematically studied by Zhang et al. [7]. The typical microstructure of the as-cast Mg-4Zn-*x*Ca (x = 0.16 and 0.56 wt %) alloys is shown in Figure 1a–c. The as-cast alloy contains the round shape particles which disperse randomly within the α-Mg matrix and the strip-like networks which tend to decorate the grain boundaries. It has been demonstrated [33,40,41] that the Mg_2Ca intermetallic phase, which is common in binary Mg-Ca alloys and ternary alloys with a higher content of Ca [42,43], does not form when the atomic ratio of Zn/Ca is greater than 1.25 and the eutectic α-Mg + $Ca_2Mg_6Zn_3$ precipitates. In good agreement with literature data, a magnified view, Figure 1c, reveals the eutectic morphology of the particles showing alternating bright and dark regions. Using the EDX technique, Figure 2, the matrix composition is found to be approximately the same in both alloys: 99.0 ± 0.1 Mg, 1.00 ± 0.04 Zn, while the composition of the precipitates, regardless of morphology, was found to be 13.1 ± 4.2 Ca, 63.6 ± 5.8 Mg, 23.3 ± 3.3 Zn in the Mg-4Zn-0.16Ca alloy and 15.1 ± 2.6 Ca, 61.4 ± 6.3 Mg, 23.5 ± 2.7 Zn (all in at %) in the Mg-4Zn-0.56Ca alloy (averaged over ten EDX spectra). This is close to the $Ca_2Mg_6Zn_3$ phase, which is commonly observed in a broad variety of Mg-Zn-Ca alloys [4,33,40,42,44]. Since the $Ca_2Mg_6Zn_3$ phase is the part of eutectic, the Mg content appears to be overestimated because of the neighborhood of the α-Mg. No signatures of other phases such as Mg_2Ca, $Ca_2Mg_5Zn_{13}$ or $Ca_2Mg_6Zn_5$, which are often discussed in the above-cited literature, were observed in the EDX spectra in the present work. The crystal structure of the secondary phase, which is morphologically similar to that shown in Figure 1c, has been investigated in detail by

electron diffraction in a transmission electron microscope in Refs. [44–47] for the Mg-Zn-Ca alloys having chemical compositions similar to those of alloys used in the present work. These studies have unequivocally shown that this phase is $Ca_2Mg_6Zn_3$, in excellent agreement with the thermodynamic analysis presented in [39]. Thus, it can be arguably concluded that the coarse secondary phase particles shown in Figure 1 are the eutectic α-Mg + $Ca_2Mg_6Zn_3$ products.

Mg alloys are "hard to deform" because of the limited number of slip systems. Therefore, to activate non-basal slip systems, promote deformation and stimulate dynamic recrystallization, hot deformation processing is common to break down the as cast structure. Lu et al. [44] have reported details of the influence of heat treatment in the temperature range from 310 to 450 °C during 24 and 48 h on the microstructure and functional properties of the Mg-3Zn-0.3Ca alloy. According to this work, annealing at 310 °C results in modest reduction of the volume fraction of the secondary phase from 2.4% to 1.7% and in only a slight increase of the grain size. The role of large particles in accelerating structural refinement during severe plastic deformation has been demonstrated based on the formation of large strain and misorientation gradients in the matrix close to these particles [48–50]. ECAP is known as an efficient technique, which is used for the breakdown of the coarse as-cast structure [51]. Based on this, the pre-ECAP annealing was performed at the temperature of 330 °C that helped to relive the internal stresses, but it was lower than that required for structure homogenization. Not surprisingly, the microstructure is still quite heterogeneous after just one ECA-pass: a large fraction of fine recrystallized grains of 2–10 μm size coexists with the coarse grains of 20–50 μm as can be seen in Figure 1d. In the present work, we do not intend to investigate the effect of deformation processing on the microstructure and mechanical properties. This should be the subject of further research. However, for the purpose of the present work, the investigated ZX40 alloys reached of 135 MPa $\sigma_{0.2}$ conventional yield stress, 276 MPa ultimate tensile strength and the excellent elongation to failure of 31% after ECAP is a good combination of strength and ductility for this class of alloys, cf. [52]. For the extruded Mg-4.0Zn-0.2Ca alloy, Sun et al. [4] have reported the yield stress of 240 MPa, tensile strength of 297 MPa and elongation to failure of 21%.

Examples of loading cycles at the largest total strain amplitude tested are shown in Figure 3. The most prominent feature of the hysteresis loops observed is their asymmetry, which is often reported for Mg alloys due to the polar nature of mechanical twinning dominating the early deformation stage [53,54]. This asymmetry manifests itself in both the different stress amplitudes in tension and compression and in the different hardening behavior during tensile and compressive parts of the hysteresis loop. Although the chosen alloys with the slightly different content of Ca exhibit somewhat different cyclic response, the main features of their deformation behavior are qualitatively similar, and these common features will be illustrated below.

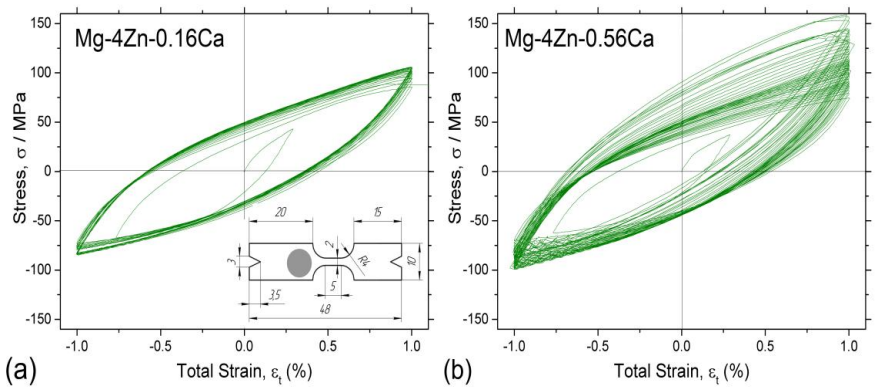

Figure 3. Hysteresis loops in the ZX40 specimens Mg-4Zn-0.16Ca (**a**); and Mg-4Zn-0.56Ca (**b**) during cyclic deformation under total strain control with the total strain amplitude $\Delta\varepsilon_t/2 = 1 \times 10^{-2}$. The specimen shape and geometry is shown in the inset. The circle indicates the location of the acoustic emision sensor.

AE data are shown in Figures 4 and 5 for both alloys in terms of AE energy E and median frequency f_m, which represent the behavior of the AE spectral density under applied load. As is commonly observed in Mg alloys, AE commences at the very low applied stress of few MPa, which agrees with low Critical Resolved Shear Stress (CRSS) values of the <a> basal dislocation slip and twinning.

As plastic deformation proceeds in either tension or compression, the AE level tends to peak near the macroscopic yield point at each loading half-cycle. The AE peak is caused by two reasons: (i) strain hardening due to dislocation accumulation reduces dislocation production rate and increases resistance for dislocation motion [55,56]; and (ii) the sine-wave signal controlling the motion of the crosshead results in a non-constant nominal strain rate that gradually reduces to zero at maximum (or minimum) stresses during loading cycles. Since the AE power (or average energy) is known to be proportional to the strain rate, it tends to reduce at the peak stress in response to the imposed strain rate. The asymmetry of the hysteresis loops is undoubtedly reflected by the dramatic difference in the AE response during tensile and compressive parts of the loading cycle. Specifically, the AE energy during compression appears to be much greater than that in tension, cf. Figures 4a and 5a.

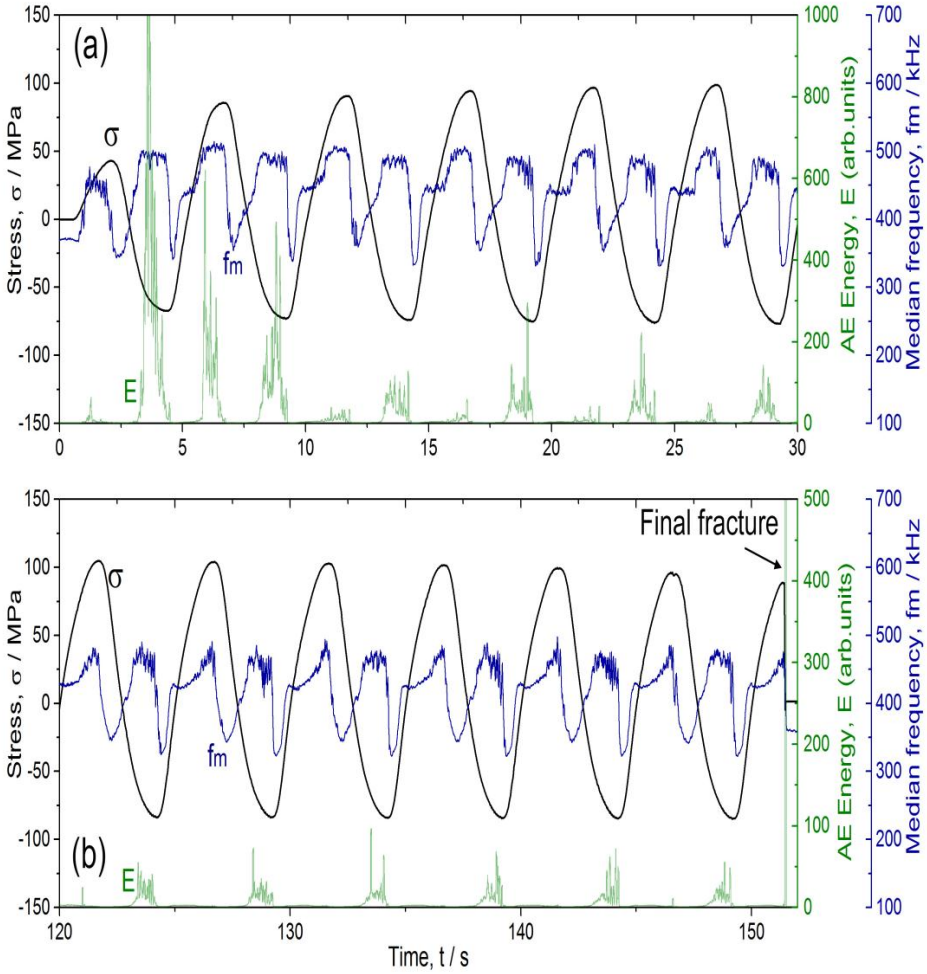

Figure 4. Acoustic emission spectral parameters—energy E and median frequency f_m of the Power Spectral Density (PSD)—plotted as a function of time during early rapid hardening stage (**a**); and late deformation stage (**b**) of the ZX40 alloy (Mg-4Zn-0.16Ca tested at $\Delta\varepsilon_t/2 = 1 \times 10^{-2}$).

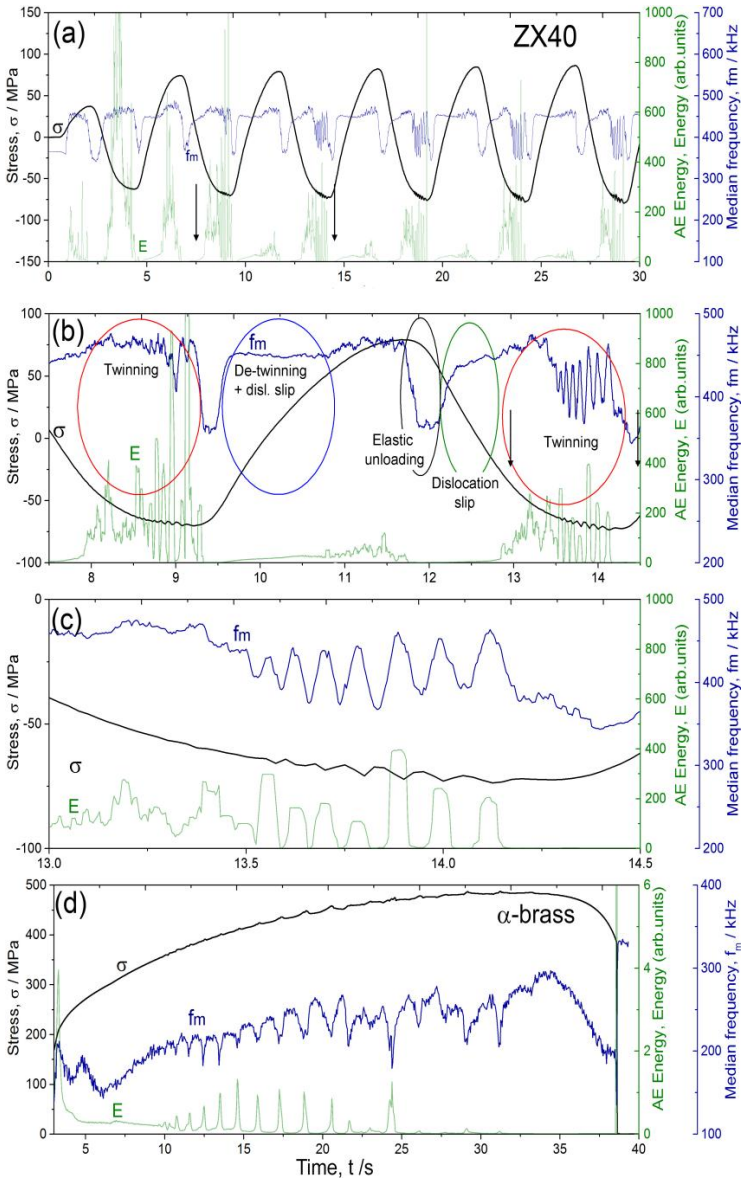

Figure 5. Acoustic emission energy E and median frequency f_m plotted as a function of time during early rapid hardening stage of the ZX40 alloy (Mg-4Zn-0.56Ca tested at $\Delta\varepsilon_t/2 = 1 \times 10^{-2}$). (**a**–**c**); (**b**) shows an enlarged fragment of data indicated on (**a**) by arrows; (**c**) shows an enlarged fragment of data indicated on (**b**); the dominating deformation mechanisms highlighted on (**b**) are identified through the cluster analysis of the AE time series; (**d**) shows the typical AE diagram obtained during monotonic deformation of α-brass exhibiting the Portevin-Le Chatelier effect due to collective dislocation motion: cf. the difference in the f_m behavior visible in (**c**,**d**) [57].

The behavior of the median frequency, which is shown in Figures 4 and 5, is similar for both specimens and is specific for deformation mechanisms operative in Mg. The details of the particular features of the f_m evolution in response to dislocation slip and twinning have been highlighted in [32] (cf. also [54,56]). One can notice that after the start of the test the AE spectral density shifts to a high frequency domain and the f_m value increases sharply as is usually observed due to dislocation production and accumulation in *fcc* and *bcc* metals and alloys [56]. The f_m value drops at the point of reversal of the loading direction, and then it starts rising again as deformation proceeds beyond a certain stress, which can be associated with a "true" yield stress and which reasonably increases as hardening proceeds. The monotonic increase in the AE median frequency

is systematically observed due to strain hardening mediated by dislocations. However, the median frequency flattens at high values on a mature stage of each cycle as the stress increases in either direction when mechanical twinning dominates the plastic flow. The similar behavior of the AE spectrum was observed in the austenitic TWIP steels where profuse twinning was observed as a dominating deformation mechanism [58]. This characteristic behavior of the AE PSD reflects the fine features of the kinetics of deformation mechanisms, which are not otherwise visible on the stress–strain diagrams. The serrated plastic flow caused by deformation twinning can, however, be observed in the Mg-4Zn-0.56Ca specimen tested at the high strain amplitude $\Delta\varepsilon_t/2 = 1 \times 10^{-2}$ (see Figure 5b) and its magnified fragment on Figure 5c. The AE energy also drops at the point of loading reversal and remains low as long as the de-twinning process is active on the tensile part of each cycle. This finding is close to the results reported in [32,54,59], where it was argued that the de-twinning process, which is systematically observed at strain path reversal in Mg polycrystals, proceeds at the velocities much slower than those at twin nucleation and is not directly detectable by AE. This can be clearly seen on the enlarged fragment of the AE time-series shown in Figure 5b. Then, the AE energy starts rising again. This rise occurs due to high amplitude AE transients generated by twins as can be best seen in Figure 5. The Mg-4Zn-0.56Ca specimen exhibits a clearly visible jerky flow when tested at larger strain amplitude of 1×10^{-2}. Serrations on the loading diagram, which are clearly resolved in Figure 5b,c, are indicative of profuse twinning which is accompanied by high amplitude AE, Figure 5c (notice that the AE amplitude is proportional to the length of the nucleated twin as shown in [60]). It is important to notice that the appearance of AE accompanying the serrated flow caused by twinning in the Mg-alloy is substantially different from the Portevin-Le Chatelier effect associated with dislocation liberation from pinning points and dynamic strain ageing. The latter effect in *fcc* alloys such as Al-Mg alloys or α-brass is also accompanied by the sharply increasing AE energy (or power) as the stress drops. However, this drop is complemented by a pronounced concomitant reduction in the AE median frequency, which occurs due to increasing correlation the moving dislocation ensembles [57]. Deformation stages are indicated schematically in Figures 5 and 6 and the corresponding deformation mechanisms are identified through the analysis of their AE response.

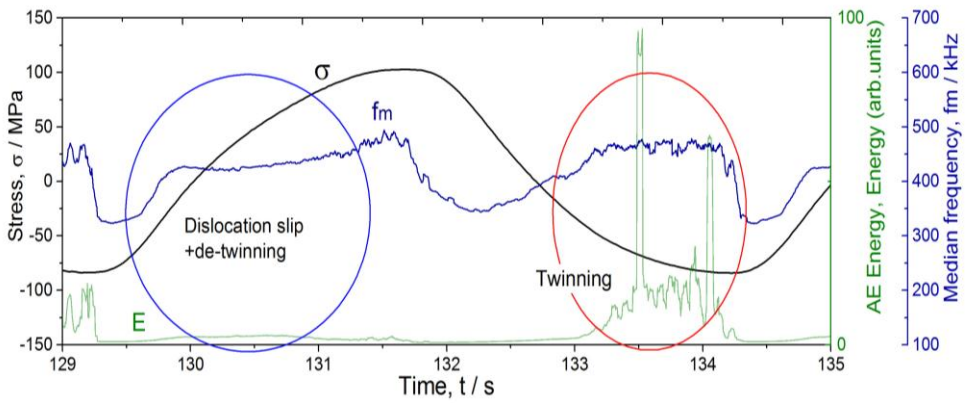

Figure 6. Enraged fragment of the AE behavior reflecting the difference in deformation mechanisms operating in successive tension and compression half-cycles on the mature stage of fatigue of the ZX40 Mg alloy (Mg-4Zn-0.16Ca tested at $\Delta\varepsilon_t/2 = 1 \times 10^{-2}$). AE signatures corresponding to twins are not seen in tension, but are still discernible in compression. Notice that the scale of the AE energy axis is ten times different from than that in Figures 4 and 5.

To observe the real-time kinetics of twinning, the raw AE signal was purified from noise. Using the ASK procedure, the fragments of AE streams having the PSD which is statistically the same as that for the background laboratory noise were automatically identified and removed from the analysis. Some occasional spurious transients, which did not form any compact cluster, were identified as outliers caused by the mechanical noise of the testing machine. These outliers were also disregarded

from the analysis. Furthermore, the signals from twinning should be discriminated from those of dislocation slip. This task is challenging yet tractable, since different AE sources generate different waveforms and therefore different Fourier power spectra at the sensor output. Applying the same ASK algorithm with a sliding window to the raw data acquired during cyclic deformation and grouping the frames with similar spectral features, allowed us to identify the signals corresponding to twinning in a way similar to that reported previously [32,54]. Figure 7 shows the results of the cluster analysis represented as the cumulative AE energy (a); and the average AE energy per cycle (b) separated for tensile and compressive stages. From Figures 4–7, one can see that, as cyclic hardening proceeds, the AE energy reduces in both tension and compression in line with common trends known for *fcc* or *bcc* metals but does not vanish completely. On the other hand, the cluster analysis undoubtedly shows (Figure 7) that twinning remains to be an active deformation mechanism (though with the admittedly decreasing energy) only during the compression part of the cycle, while it ceases to operate during tension at later stages of fatigue. This analysis is corroborated by visual inspection of the AE behavior at the late deformation stage, cf. Figure 6, where the AE signal corresponding to twinning can be seen only during the compression part of the cycle. Final fracture has always been reasonably observed during the ascending part of the hysteresis cycle close to the peak tensile stress. The observed behavior of the deformation mechanisms allows for suggesting that fracture occurs when the imposed tensile plastic strains cannot be accommodated by main complementary mechanisms—basal slip and twinning. When the twinning is exhausted, the slip dominates the cyclic deformation process. However, the "hard" deformation modes (i.e., prismatic or pyramidal dislocation slip) are unlikely to be activated under the current loading conditions since the stress amplitude is still low. Therefore, since basal slip alone cannot accommodate large cumulative strains, the final crack nucleates and propagates quickly, causing fatal fatigue failure of the examined Mg ZX40 alloys.

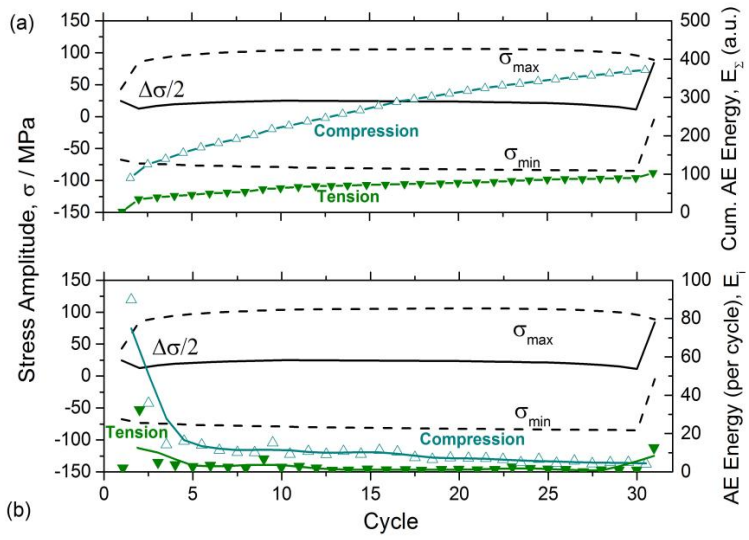

Figure 7. Trends in the twinning behavior assessed by the cluster analysis of AE time series in tension and compression during cyclic deformation of the Mg-4Zn-0.16Ca alloy tested at $\Delta\varepsilon_t/2 = 1 \times 10^{-2}$: (**a**) shows the cumulative AE energy and (**b**) the average AE energy per cycle.

4. Conclusions

Using the robust analysis of AE time series during low cyclic fatigue testing of the Mg-Zn-Ca alloys, the behavior of primary deformation modes—basal slip and twinning—has been clarified with respect to the direction and time of loading. Fine details of the interaction between dislocation slip and twinning are encoded in the AE signal and be disclosed by means of the spectral and cluster analysis of the continuously recorded AE signal.

The kinetics of twin accumulation in tension and compression per cycle and the overall accumulation of twinning during cyclic loading is described and its effect on fatigue life is highlighted. Specifically, using the non-destructive AE technique, it was undoubtedly demonstrated that twinning in tension tends to saturate significantly faster than that in compression. The observed behavior of deformation mechanisms indicates that a fatigue fracture occurs when the imposed tensile plastic strains can not be accommodated by main deformation mechanisms—basal slip and twinning once the latter is exhausted in the course of cyclic deformation.

Acknowledgments: Financial support from the Russian Science Foundation through the grant-in-aid No. 15-19-30025 is gratefully appreciated.

Author Contributions: A.V. devised the experiments, analyzed AE data and wrote the paper, E.V. and M.L. performed the experiments and analyzed the AE data, D.M. discussed the results.

Conflicts of Interest: The authors declare no conflict of interest.

References

1. Bettles, C.; Barnett, M. *Advances in Wrought Magnesium Alloys: Fundamentals of Processing, Properties and Applications*; Woodhead Publishing Ltd.: Philadelphia, PA, USA, 2012; pp. 1–463.
2. Xin, Y.; Hu, T.; Chu, P.K. In vitro studies of biomedical magnesium alloys in a simulated physiological environment: A review. *Acta Biomater.* **2011**, *7*, 1452–1459. [CrossRef] [PubMed]
3. Witte, F. The history of biodegradable magnesium implants: A review. *Acta Biomater.* **2010**, *6*, 1680–1692. [CrossRef] [PubMed]
4. Sun, Y.; Zhang, B.; Wang, Y.; Geng, L.; Jiao, X. Preparation and characterization of a new biomedical Mg-Zn-Ca alloy. *Mater. Des.* **2012**, *34*, 58–64. [CrossRef]
5. Hofstetter, J.; Becker, M.; Martinelli, E.; Weinberg, A.M.; Mingler, B.; Kilian, H.; Pogatscher, S.; Uggowitzer, P.J.; Löffler, J.F. High-strength low-alloy (HSLA) Mg-Zn-Ca alloys with excellent biodegradation performance. *JOM* **2014**, *66*, 566–572. [CrossRef]
6. Hofstetter, J.; Martinelli, E.; Pogatscher, S.; Schmutz, P.; Povoden-Karadeniz, E.; Weinberg, A.M.; Uggowitzer, P.J.; Löffler, J.F. Influence of trace impurities on the in vitro and in vivo degradation of biodegradable Mg-5Zn-0.3Ca alloys. *Acta Biomater.* **2015**, *23*, 347–353. [CrossRef] [PubMed]
7. Zhang, B.P.; Wang, Y.; Geng, L. *Research on Mg-Zn-Ca Alloy as Degradable Biomaterial, Biomaterials—Physics and Chemistry*; Pignatello, R., Ed.; InTech.: Rijeka, Croatia, 2011.
8. Barnett, M.R. Twinning and the ductility of magnesium alloys. Part I: "Tension" twins. *Mater. Sci. Eng. A* **2007**, *464*, 1–7. [CrossRef]
9. Barnett, M.R. Twinning and the ductility of magnesium alloys. Part II. "Contraction" twins. *Mater. Sci. Eng. A* **2007**, *464*, 8–16. [CrossRef]
10. Barnett, M.R. Twinning and its role in wrought magnesium alloys. In *Advances in Wrought Magnesium Alloys: Fundamentals of Processing, Properties and Applications*; Bettles, C., Barnett, M., Eds.; Elsevier: Amsterdam, The Netherlands, 2012; pp. 105–143.
11. Barnett, M.R. Texture, twinning and uniform elongation of wrought magnesium. *Mater. Sci. Forum* **2005**, *495–497*, 1079–1084. [CrossRef]
12. Stanford, N.; Sotoudeh, K.; Bate, P.S. Deformation mechanisms and plastic anisotropy in magnesium alloy AZ31. *Acta Mater.* **2011**, *59*, 4866–4874. [CrossRef]
13. Xin, Y.; Wang, M.; Zeng, Z.; Nie, M.; Liu, Q. Strengthening and toughening of magnesium alloy by {10−12} extension twins. *Scr. Mater.* **2012**, *66*, 25–28. [CrossRef]
14. Wu, L.; Agnew, S.R.; Ren, Y.; Brown, D.W.; Clausen, B.; Stoica, G.M.; Wenk, H.R.; Liaw, P.K. The effects of texture and extension twinning on the low-cycle fatigue behavior of a rolled magnesium AZ31b. *Mater. Sci. Eng. A* **2010**, *527*, 7057–7067. [CrossRef]
15. Agnew, S.R.; Duygulu, O. Plastic anisotropy and the role of non-basal slip in magnesium alloy AZ31b. *Int. J. Plast.* **2005**, *21*, 1161–1193. [CrossRef]
16. Chapuis, A.; Driver, J.H. Temperature dependency of slip and twinning in plane strain compressed magnesium single crystals. *Acta Mater.* **2011**, *59*, 1986–1994. [CrossRef]

17. Khan, A.S.; Pandey, A.; Gnaupel-Herold, T.; Mishra, R.K. Mechanical response and texture evolution of AZ31 alloy at large strains for different strain rates and temperatures. *Int. J. Plast.* **2011**, *27*, 688–706. [CrossRef]
18. Yu, Q.; Zhang, J.; Jiang, Y. Direct observation of twinning-detwinning-retwinning on magnesium single crystal subjected to strain-controlled cyclic tension-compression in [0001] direction. *Philos. Mag. Lett.* **2011**, *91*, 757–765. [CrossRef]
19. Roberts, C.S. *Magnesium and Its Alloys*; Wiley: New York, NY, USA, 1960; p. 230.
20. Proust, G.; Tomé, C.N.; Jain, A.; Agnew, S.R. Modeling the effect of twinning and detwinning during strain-path changes of magnesium alloy AZ31. *Int. J. Plast.* **2009**, *25*, 861–880. [CrossRef]
21. Čapek, J.; Máthis, K.; Clausen, B.; Stráská, J.; Beran, P.; Lukáš, P. Study of the loading mode dependence of the twinning in random textured cast Mg by acoustic emission and neutron diffraction methods. *Mater. Sci. Eng. A* **2014**, *602*, 25–32. [CrossRef]
22. Mirza, F.A.; Chen, D.L.; Li, D.J.; Zeng, X.Q. Low cycle fatigue of a rare-earth containing extruded magnesium alloy. *Mater. Sci. Eng. A* **2013**, *575*, 65–73. [CrossRef]
23. Yin, S.M.; Wang, C.H.; Diao, Y.D.; Wu, S.D.; Li, S.X. Influence of grain size and texture on the yield asymmetry of Mg-3Al-1Zn alloy. *J. Mater. Sci. Technol.* **2011**, *27*, 29–34. [CrossRef]
24. Lou, X.Y.; Li, M.; Boger, R.K.; Agnew, S.R.; Wagoner, R.H. Hardening evolution of AZ31b Mg sheet. *Int. J. Plast.* **2007**, *23*, 44–86. [CrossRef]
25. Pomponi, E.; Vinogradov, A. A real-time approach to acoustic emission clustering. *Mech. Syst. Signal Proc.* **2013**, *40*, 791–804. [CrossRef]
26. Vinogradov, A.; Orlov, D.; Danyuk, A.; Estrin, Y. Effect of grain size on the mechanisms of plastic deformation in wrought Mg-Zn-Zr alloy revealed by acoustic emission measurements. *Acta Mater.* **2013**, *61*, 2044–2056. [CrossRef]
27. Máthis, K.; Csiszár, G.; Čapek, J.; Gubicza, J.; Clausen, B.; Lukáš, P.; Vinogradov, A.; Agnew, S.R. Effect of the loading mode on the evolution of the deformation mechanisms in randomly textured magnesium polycrystals—Comparison of experimental and modeling results. *Int. J. Plast.* **2015**, *72*, 127–150. [CrossRef]
28. Linderov, M.; Segel, C.; Weidner, A.; Biermann, H.; Vinogradov, A. Deformation mechanisms in austenitic TRIP/TWIP steels at room and elevated temperature investigated by acoustic emission and scanning electron microscopy. *Mater. Sci. Eng. A* **2014**, *597*, 183–193. [CrossRef]
29. Takeda, R.; Kaneko, Y.; Merson, D.L.; Vinogradov, A. Cluster analysis of acoustic emissions measured during deformation of duplex stainless steels. *Mater. Trans.* **2013**, *54*, 532–539. [CrossRef]
30. Kádár, C.; Máthis, K.; Orbulov, I.N.; Chmelík, F. Monitoring the failure mechanisms in metal matrix syntactic foams during compression by acoustic emission. *Mater. Lett.* **2016**, *173*, 31–34. [CrossRef]
31. Vinogradov, A.; Nadtochiy, M.; Hashimoto, S.; Miura, S. Correlation between spectral parameters of acoustic-emission during plastic-deformation of Cu and Cu-Al single and polycrystals. *Mater. Trans. JIM* **1995**, *36*, 426–431. [CrossRef]
32. Vinogradov, A.; Orlov, D.; Danyuk, A.; Estrin, Y. Deformation mechanisms underlying tension-compression asymmetry in magnesium alloy ZK60 revealed by acoustic emission monitoring. *Mater. Sci. Eng. A* **2015**, *621*, 243–251. [CrossRef]
33. Zhang, B.; Hou, Y.; Wang, X.; Wang, Y.; Geng, L. Mechanical properties, degradation performance and cytotoxicity of Mg-Zn-Ca biomedical alloys with different compositions. *Mater. Sci. Eng. C* **2011**, *31*, 1667–1673. [CrossRef]
34. Baker, H. *Alloy Phase Diagrams*; ASM International: Materials Park, OH, USA, 1992.
35. Mezbahul-Islam, M.; Mostafa, A.O.; Medraj, M. Essential magnesium alloys binary phase diagrams and their thermochemical data. *J. Mater.* **2014**, *2014*, 704283. [CrossRef]
36. Clark, J.B. The solid constitution in the Mg-rich region of the Mg-Zn-Ca phase diagram. In *Transactions of the Metallurgical Society of AIME*; AIME: New York, NY, USA, 1961; Volume 221, pp. 644–645.
37. Levi, G.; Avraham, S.; Zilberov, A.; Bamberger, M. Solidification, solution treatment and age hardening of a Mg-1.6Ca-3.2Zn alloy. *Acta Mater.* **2006**, *54*, 523–530. [CrossRef]
38. Bakhsheshi-Rad, H.R.; Hamzah, E.; Fereidouni-Lotfabadi, A.; Daroonparvar, M.; Yajid, M.A.M.; Mezbahul-Islam, M.; Kasiri-Asgarani, M.; Medraj, M. Microstructure and bio-corrosion behavior of Mg-Zn and Mg-Zn-Ca alloys for biomedical applications. *Mater. Corros.* **2014**, *65*, 1178–1187. [CrossRef]
39. Wasiur-Rahman, S.; Medraj, M. Critical assessment and thermodynamic modeling of the binary Mg-Zn, Ca-Zn and ternary Mg-Ca-Zn systems. *Intermetallics* **2009**, *17*, 847–864. [CrossRef]

40. Larionova, T.V.; Park, W.-W.; You, B.-S. A ternary phase observed in rapidly solidified Mg-Ca-Zn alloys. *Scr. Mater.* **2001**, *45*, 7–12. [CrossRef]
41. Yin, P.; Li, N.F.; Lei, T.; Liu, L.; Ouyang, C. Effects of ca on microstructure, mechanical and corrosion properties and biocompatibility of Mg-Zn-Ca alloys. *J. Mater. Sci. Mater. Med.* **2013**, *24*, 1365–1373. [CrossRef] [PubMed]
42. Zhou, T.; Chen, D.; Chen, Z.H. Microstructures and properties of rapidly solidified Mg-Zn-Ca alloys. *Trans. Nonferr. Met. Soc. China* **2008**, *18*, S101–S106. [CrossRef]
43. Doležal, P.; Zapletal, J.; Fintová, S.; Trojanová, Z.; Greger, M.; Roupcová, P.; Podrábský, T. Influence of processing techniques on microstructure and mechanical properties of a biodegradable Mg-3Zn-2Ca alloy. *Materials* **2016**, *9*, 880. [CrossRef]
44. Lu, Y.; Bradshaw, A.R.; Chiu, Y.L.; Jones, I.P. Effects of secondary phase and grain size on the corrosion of biodegradable Mg-Zn-Ca alloys. *Mater. Sci. Eng. C* **2015**, *48*, 480–486. [CrossRef] [PubMed]
45. Kubok, K.; Lityńska-Dobrzyńska, L.; Wojewoda-Budka, J.; Góral, A.; Dębski, A. Investigation of structures in as-cast alloys from the Mg-Zn-Ca system. *Arch. Metall. Mater.* **2013**, *58*, 329–333. [CrossRef]
46. Jardim, P.M.; Solórzano, G.; Sande, J.B.V. Precipitate crystal structure determination in melt spun Mg-1.5Ca-6Zn alloy. *Microsc. Microanal.* **2002**, *8*, 487–496. [CrossRef] [PubMed]
47. Tong, L.B.; Zheng, M.Y.; Kamado, S.; Zhang, D.P.; Meng, J.; Cheng, L.R.; Zhang, H.J. Reducing the tension-compression yield asymmetry of extruded Mg-Zn-Ca alloy via equal channel angular pressing. *J. Magnes. Alloy.* **2015**, *3*, 302–308. [CrossRef]
48. Humphreys, F.J. Local lattice rotations at second phase particles in deformed metals. *Acta Metall.* **1979**, *27*, 1801–1814. [CrossRef]
49. Gutierrez-Urrutia, I.; Munoz-Morris, M.A.; Morris, D.G. Contribution of microstructural parameters to strengthening in an ultrafine-grained Al-7%Si alloy processed by severe deformation. *Acta Mater.* **2007**, *55*, 1319–1330. [CrossRef]
50. Humphreys, J.; Bate, P. Gradient plasticity and deformation structures around inclusions. *Scr. Mater.* **2003**, *48*, 173–178. [CrossRef]
51. Chung, C.W.; Ding, R.G.; Chiu, Y.L.; Hodgson, M.A.; Gao, W. Microstructure and mechanical properties of an as-cast AZ91 magnesium alloy processed by ECAP. *IOP Conf. Ser. Mater. Sci. Eng.* **2009**, *4*, 012012. [CrossRef]
52. Geng, L.; Zhang, B.P.; Li, A.B.; Dong, C.C. Microstructure and mechanical properties of Mg-4.0Zn-0.5Ca alloy. *Mater. Lett.* **2009**, *63*, 557–559. [CrossRef]
53. Lee, S.; Wang, H.; Gharghouri, M. Twinning-detwinning behavior during cyclic deformation of magnesium alloy. *Metals* **2015**, *5*, 881–890. [CrossRef]
54. Vinogradov, A.; Vasilev, E.; Linderov, M.; Merson, D. In situ observations of the kinetics of twinning-detwinning and dislocation slip in magnesium. *Mater. Sci. Eng. A* **2016**, *676*, 351–360. [CrossRef]
55. Vinogradov, A.; Yasnikov, I.S. On the nature of acoustic emission and internal friction during cyclic deformation of metals. *Acta Mater.* **2014**, *70*, 8–18. [CrossRef]
56. Vinogradov, A.; Yasnikov, I.S.; Estrin, Y. Stochastic dislocation kinetics and fractal structures in deforming metals probed by acoustic emission and surface topography measurements. *J. Appl. Phys.* **2014**, *115*, 233506. [CrossRef]
57. Vinogradov, A.; Lazarev, A. Continuous acoustic emission during intermittent plastic flow in α-brass. *Scr. Mater.* **2012**, *66*, 745–748. [CrossRef]
58. Vinogradov, A.; Lazarev, A.; Linderov, M.; Weidner, A.; Biermann, H. Kinetics of deformation processes in high-alloyed cast TRIP/TWIP steels determined by acoustic emission and scanning electron microscopy. *Acta Mater.* **2013**, *61*, 2434–2449. [CrossRef]
59. Drozdenko, D.; Bohlen, J.; Yi, S.; Minárik, P.; Chmelík, F.; Dobroň, P. Investigating a twinning-detwinning process in wrought Mg alloys by the acoustic emission technique. *Acta Mater.* **2016**, *110*, 103–113. [CrossRef]
60. Vinogradov, A.; Vasilev, E.; Seleznev, M.; Máthis, K.; Orlov, D.; Merson, D. On the limits of acoustic emission detectability for twinning. *Mater. Lett.* **2016**, *183*, 417–419. [CrossRef]

© 2016 by the authors; licensee MDPI, Basel, Switzerland. This article is an open access article distributed under the terms and conditions of the Creative Commons Attribution (CC-BY) license (http://creativecommons.org/licenses/by/4.0/).